Publications of the Astronomical Society of the Pacific, 131:014002 (16pp), 2019 January https://doi.org/10.1088/1538-3873/aae961

Carnegie Supernova Project-II: The Near-infrared Spectroscopy Program*

E. Y. Hsiao (蕭亦麒)[1], M. M. Phillips[2], G. H. Marion[3], R. P. Kirshner[4,5], N. Morrell[2], D. J. Sand[6], C. R. Burns[7], C. Contreras[2], P. Hoeflich[1], M. D. Stritzinger[8], S. Valenti[9], J. P. Anderson[10], C. Ashall[1], C. Baltay[11], E. Baron[12], D. P. K. Banerjee[13], S. Davis[1], T. R. Diamond[14], G. Folatelli[15], Wendy L. Freedman[16], F. Förster[17,18], L. Galbany[19], C. Gall[20], S. González-Gaitán[21], A. Goobar[22], M. Hamuy[18], S. Holmbo[8], M. M. Kasliwal[23], K. Krisciunas[24], S. Kumar[1], C. Lidman[25], J. Lu[1], P. E. Nugent[26,27], S. Perlmutter[26,27], S. E. Persson[7], A. L. Piro[7], D. Rabinowitz[11], M. Roth[2,28], S. D. Ryder[29], B. P. Schmidt[30], M. Shahbandeh[1], N. B. Suntzeff[24], F. Taddia[31], S. Uddin[7], and L. Wang[32,33]

[1] Department of Physics, Florida State University, 77 Chieftan Way, Tallahassee, FL 32306, USA; ehsiao@fsu.edu
[2] Carnegie Observatories, Las Campanas Observatory, Colina El Pino, Casilla 601, Chile
[3] Department of Astronomy, University of Texas, 1 University Station C1400, Austin, TX 78712, USA
[4] Harvard-Smithsonian Center for Astrophysics, 60 Garden Street, Cambridge, MA 02138, USA
[5] Gordon and Betty Moore Foundation, 1661 Page Mill Road, Palo Alto, CA 94304, USA
[6] Department of Astronomy and Steward Observatory, University of Arizona, 933 N. Cherry Avenue, Tucson, AZ 85719, USA
[7] Observatories of the Carnegie Institution for Science, 813 Santa Barbara Street, Pasadena, CA 91101, USA
[8] Department of Physics and Astronomy, Aarhus University, Ny Munkegade, DK-8000 Aarhus C, Denmark
[9] Department of Physics, University of California, Davis, CA 95616, USA
[10] European Southern Observatory, Alonso de Córdova 3107, Casilla 19, Santiago, Chile
[11] Physics Department, Yale University, 217 Prospect Street, New Haven, CT 06511, USA
[12] Homer L. Dodge Department of Physics and Astronomy, 440 West Brooks Street, Room 100, Norman, OK 73019, USA
[13] Astronomy and Astrophysics Division, Physical Research Laboratory, Navrangapura, Ahmedabad—380009, Gujarat, India
[14] Laboratory of Observational Cosmology, Code 665, NASA Goddard Space Flight Center, Greenbelt, MD 20771, USA
[15] Facultad de Ciencias Astronómicas y Geofísicas, Universidad Nacional de La Plata, Instituto de Astrofísica de La Plata (IALP), CONICET, Paseo del Bosque S/N, B1900FWA La Plata, Argentina
[16] Department of Astronomy and Astrophysics, University of Chicago, 5640 Ellis Avenue Chicago, IL 60637, USA
[17] Millennium Institute of Astrophysics, Casilla 36-D,7591245, Santiago, Chile
[18] Departamento de Astronomía, Universidad de Chile, Casilla 36-D, Santiago, Chile
[19] PITT PACC, Department of Physics and Astronomy, University of Pittsburgh, Pittsburgh, PA 15260, USA
[20] Dark Cosmology Centre, Niels Bohr Institute, University of Copenhagen, Juliane Maries Vej 30, 2100 Copenhagen, Denmark
[21] CENTRA—Centro de Astrofísica e Gravitação, Instituto Superior Técnico, Av. Rovisco Pais 1, 1049-001, Lisbon, Portugal
[22] The Oskar Klein Centre, Department of Physics, Stockholm University, AlbaNova, 10691 Stockholm, Sweden
[23] 4Division of Physics, Mathematics and Astronomy, California Institute of Technology, Pasadena, California 91125, USA
[24] George P. and Cynthia Woods Mitchell Institute for Fundamental Physics and Astronomy, Department of Physics and Astronomy, Texas A&M University, College Station, TX, 77843, USA
[25] The Research School of Astronomy and Astrophysics, Australian National University, ACT 2601, Australia
[26] Lawrence Berkeley National Laboratory, Department of Physics, 1 Cyclotron Road, Berkeley, CA 94720, USA
[27] Astronomy Department, University of California at Berkeley, Berkeley, CA 94720, USA
[28] GMTO Corporation, Avenida Presidente Riesco 5335, Suite 501, Las Condes, Santiago, Chile
[29] Department of Physics & Astronomy, Macquarie University, NSW 2109, Australia
[30] Research School of Astronomy and Astrophysics, The Australian National University, Weston, ACT 2611, Australia
[31] The Oskar Klein Centre, Department of Astronomy, Stockholm University, AlbaNova, 10691 Stockholm, Sweden
[32] Key Laboratory of Optical Astronomy, National Astronomical Observatories, Chinese Academy of Sciences, Beijing 100012, People's Republic of China
[33] Chinese Academy of Sciences South America Center for Astronomy, China-Chile Joint Center for Astronomy, Camino El Observatorio 1515, Las Condes, Santiago, Chile

Received 2018 September 19; accepted 2018 October 17; published 2018 November 27

Abstract

Shifting the focus of Type Ia supernova (SN Ia) cosmology to the near infrared (NIR) is a promising way to significantly reduce the systematic errors, as the strategy minimizes our reliance on the empirical width-luminosity relation and uncertain dust laws. Observations in the NIR are also crucial for our understanding of the origins and evolution of these events, further improving their cosmological utility. Any future experiments in the rest-frame NIR will require knowledge of the SN Ia NIR spectroscopic diversity, which is currently based on a small sample of observed spectra. Along with the accompanying paper, Phillips et al., we introduce the Carnegie Supernova Project-II (CSP-II), to follow-up nearby SNe Ia in both the optical and the NIR. In particular, this paper focuses on the CSP-II NIR spectroscopy program, describing the survey strategy, instrumental setups, data reduction, sample characteristics, and future analyses on the data set. In collaboration with the Harvard-Smithsonian Center for Astrophysics (CfA) Supernova Group, we obtained 661 NIR spectra of 157 SNe Ia. Within this sample, 451 NIR

* This paper includes data gathered with the 6.5-m Magellan telescopes at Las Campanas Observatory, Chile.

spectra of 90 SNe Ia have corresponding CSP-II follow-up light curves. Such a sample will allow detailed studies of the NIR spectroscopic properties of SNe Ia, providing a different perspective on the properties of the unburned material; the radioactive and stable nickel produced; progenitor magnetic fields; and searches for possible signatures of companion stars.

Key words: (stars:) supernovae: general – (cosmology:) dark energy

1. Introduction

The surprising discovery of the accelerated expansion of the universe was based on observations of Type Ia supernovae (SNe Ia; Riess et al. 1998; Perlmutter et al. 1999). Understanding the underlying cause of this "dark energy" ranks as one of the critical tasks of contemporary physics. SNe Ia remain the most direct probes, and when combined with complementary techniques, such as cosmic microwave background and baryon acoustic oscillations, provide crucial limits on the dark-energy equation of state parameter (e.g., Betoule et al. 2014; Scolnic et al. 2018).

SN Ia cosmology has however reached an impasse. It is currently limited by systematic errors (e.g., Conley et al. 2011; Suzuki et al. 2012), and increasing the sample size does not improve the situation. Despite years of significant efforts, making progress in reducing these errors has proved difficult. While shifting observations to the near infrared (NIR) is technically more challenging (e.g., more affected by telluric absorption and fewer high precision photometric standards), it offers a promising way forward in two separate respects: (1) by effectively circumventing the empirical relations that SN Ia cosmology relies upon, such as dust laws and luminosity-light-curve-shape relations and (2) by systematically exploring the NIR window to understand the physics of these explosions.

While SNe Ia are "standardizable" candles in the optical following the width–luminosity relation, in the sense that fainter SNe Ia have faster declining light curves (Phillips 1993), they are close to being standard candles in the NIR (e.g., Krisciunas et al. 2004; Folatelli et al. 2010; Kattner et al. 2012). Fainter SNe Ia also have lower temperatures radiating a higher percentage of their energy at redder wavelengths. This effect serendipitously creates a regulating mechanism, which produces near-constant peak magnitudes in the NIR (Kasen 2006). Shifting observations to the rest-frame NIR reduces our reliance on an empirical width-luminosity relation. Furthermore, color corrections due to dust and any systematic errors associated with these, are much smaller in the NIR compared with the optical, avoiding the reliance on uncertain dust extinction laws.

There is a consensus that SNe Ia are thermonuclear disruptions of carbon–oxygen white dwarfs. However, beyond that, the origins of these explosions are uncertain. The companion star can be a non-degenerate star: a main sequence, helium, or red giant star, in a single-degenerate system (Whelan & Iben 1973; Nomoto 1982), or another white dwarf in a double-generate system (Iben & Tutukov 1984; Webbink 1984). Independent of the progenitor systems, the triggering mechanism is also under debate. For example, when the mass of a carbon–oxygen white dwarf approaches the Chandrasekhar mass, the explosion can be triggered near the center by compressional heating. For this mechanism, a transition of the nuclear flame front from deflagration to detonation (DDT; Khokhlov 1991) appears to match observations well (e.g., Höflich 1995; Wheeler et al. 1998). Scenarios that trigger explosions in sub-Chandrasekhar-mass white dwarfs have also been proposed. For example, in a helium detonation scenario, the surface He layer of a sub-Chandrasekhar-mass white dwarf is detonated, which in turn drives a shock wave that subsequently detonates near the center of the white dwarf (e.g., Fink et al. 2010). It is currently unclear whether the population of SNe Ia used for cosmological studies is composed of explosions of a single triggering mechanism (Hoeflich et al. 2017) or multiple (Blondin et al. 2017) ones. Because of these uncertainties, incorporating or reducing associated systematics is not straightforward.

The NIR carries independent information in both light curves and spectra (e.g., Mandel et al. 2011; Hsiao et al. 2013). In particular, it is easier to distinguish varying distributions of intermediate-mass elements near maximum and of iron-group elements past maximum in the NIR compared with the optical. The NIR lines have moderate optical depth (Wheeler et al. 1998; Höflich et al. 2002) in contrast to, for example, the often saturated Ca and Si lines in the optical (e.g., Hachinger et al. 2008). These NIR lines then offer many clues to the physics of these explosions. The approach of the Carnegie Supernova Project (CSP-I) was to emphasize the NIR, and the second phase (CSP-II) was no different.

The CSP-I was an NSF-funded project to obtain optical and NIR light curves of SNe Ia in a well-defined and understood photometric system (Hamuy et al. 2006). It ran from 2004 to 2009, and followed more than 123 nearby SNe Ia (Contreras et al. 2010; Stritzinger et al. 2011; Krisciunas et al. 2017), as well as SNe of other types (e.g., Stritzinger et al. 2018), with rapid cadence and high photometric precision. With this data set, CSP-I established a low-redshift anchor on the Hubble diagram and provided physical insights into these explosions. However, a sizable fraction of the SNe Ia obtained in CSP-I was not in the smooth Hubble flow, and therefore they were susceptible to large peculiar velocity errors that are comparable

with the intrinsic dispersion we are investigating. The solution is to observe SNe Ia in the Hubble flow, as Barone-Nugent et al. (2012) did for a dozen SNe Ia at $0.03 < z < 0.09$. In the H band, they found a very encouraging result of a 0.085 mag scatter in the peak magnitude or 4% uncertainty in distance, even with rudimentary K-corrections applied. More recently, Stanishev et al. (2018) also confirmed the utility of distant SNe Ia in the NIR, using 16 SNe Ia with single-epoch NIR photometric observations out to a redshift of $z = 0.183$. Their K-corrections were derived from previously published NIR spectra of 10 SNe Ia.

CSP-II was a four-year NSF-supported follow-up program that ran from 2011 to 2015. The main goals were to obtain optical and NIR light curves of a "Cosmology" sample of SNe Ia in the smooth Hubble flow, and to obtain optical and NIR spectra, as well as accompanying optical and NIR light curves of a "Physics" sample of nearby SNe Ia to improve the NIR K-corrections and to improve our understanding of these events. Several instrumental improvements were made between CSP-I and CSP-II, which helped in these goals (see Phillips et al. 2018 for details). The optical imager on the 1-m Swope telescope was upgraded. The RetroCam NIR imager was moved from the 1-m Swope to the 2.5-m du Pont telescope allowing observations of SNe Ia located out in the Hubble flow. Two instruments, both mounted on the 6.5-m Magellan Baade telescope, were newly commissioned at the start of CSP-II: the NIR spectrometer, the Folded-port InfraRed Echellette (FIRE; Simcoe et al. 2013), and the NIR imager, FourStar (Persson et al. 2013). During CSP-I, observations with the Magellan telescopes were used to construct a rest-frame I-band Hubble diagram of high-redshift SNe Ia (Freedman et al. 2009). In CSP-II, the Magellan telescope observations were entirely dedicated to the low-redshift survey, mainly to obtain NIR spectra with FIRE. Observations ran from October to May, coinciding with the Chilean summer, when photometric conditions are present on >70% of the nights at the Las Campanas Observatory (LCO).

In this paper, we introduce the NIR spectroscopy program and the "Physics" sample of CSP-II; while in an accompanying paper, Phillips et al. (2018), a general overview of the CSP-II with emphasis on the imaging observations, is presented. In Section 2, the observations are described, including the instruments used and the reduction methods applied. In Section 3, we describe our sample. In Sections 4 and 5, we describe the use of this sample to improve K-corrections and our understanding of the physics of these explosions, respectively. A summary is then presented in Section 6.

2. Observations and Data Reductions

In this section, we describe the instrumental settings and data reduction for the main instruments we used to obtain NIR spectra for this program. A wide range of instruments allows the follow-up of supernovae at a range of magnitudes. The low-resolution modes of FIRE, GNIRS, and FLAMINGOS-2 are capable of obtaining spectra with $S/N \gtrsim 20$ of objects brighter than $H \sim 19$–20 mag. The prism mode of SpeX is capable of reaching the same S/N with objects brighter than $H \sim 17$–18 mag.

2.1. FIRE

As seen in Table 2, FIRE at the LCO 6.5-m Magellan Baade Telescope was the main workhorse for the CSP-II NIR spectroscopy program. It was newly commissioned and released for general use in the 2010B semester. Three nights of test runs were conducted in the 2011A semester to determine the optimal observational setup for supernovae. Several SNe Ia were observed during the test runs, including the SN 2002cx-like SN 2011ce, although these test observations do not have accompanying CSP-II light curves. The CSP-II began in the 2011B semester.

The majority of FIRE spectra were obtained in the high-throughput prism mode with a $0\farcs6$ slit. This configuration yields continuous wavelength coverage from 0.8 to 2.5 μm, with resolutions of $R \sim 500$, 450, and 300 in the JHK bands, respectively. Only a handful of nearby SNe Ia (within 20 Mpc) were observed in the high-resolution echellette mode, which yields a resolution of $R = 6000$. When acquiring a target, the slit was oriented along the parallactic angle to minimize the effect of differential refraction (Filippenko 1982). For each science observation, an A0V star close to the science observation in time, angular distance, and air mass was observed as the telluric and flux standard. For each science or telluric observation, several frames (>4) were obtained using the conventional ABBA "nod-along-the-slit" technique. The "sampling-up-the-ramp" readout mode was chosen for the science exposures to reduce the readout noise through the sampling of multiple non-destructive reads. The per-frame exposure time was typically ~2 minutes or shorter, depending on the brightness of the supernova. These exposure times were chosen such that an adequate signal was obtained in each frame without saturating the detector with airglow emissions in the JHK bands and thermal background, mostly affecting the red side of K band. For each science and telluric observation, a spectrum was taken of Ne and Ar arc lamps for wavelength calibration. The "low gain" mode of 3.8 e−/DN for the detector gain setting was always chosen to avoid saturation of the A0V telluric standards, which were typically between 10 to 12 mag.

The data were reduced using the IDL pipeline `firehose` (Simcoe et al. 2013), specifically designed for the reduction of FIRE data. The pipeline performed steps of flat fielding, wavelength calibration, sky subtraction, spectral tracing, and extraction. Wavelength calibration was done using ~40 Ne/Ar lines, which are evenly spaced out in pixel space. The

wavelength solutions typically yielded 2–6 Å rms dispersion from the blue end to the red end, and a 4 Å rms dispersion overall. For the removal of sky lines and background, the background flux was modeled using off-source pixels as described by Kelson (2003) and subtracted from each frame, instead of the conventional A-B pair subtractions. This step removed the host-galaxy background in the cases of moderate host contamination. No further steps were taken to subtract host-galaxy light. The spectral extraction was then performed using the optimal extraction technique (Horne 1986), a weighting scheme that maximizes the signal-to-noise ratio (S/N) while preserving spectrophotometric accuracy. We took advantage of the multiple spectra to perform sigma clipping to reject spurious pixels, and also to produce an error spectrum by computing the standard deviation at each pixel. Individual 1D spectra were then median combined. Corrections for telluric absorptions were performed using the IDL tool `xtellcor` developed by Vacca et al. (2003). To construct a telluric correction spectrum free of stellar absorption features, a model spectrum of Vega was used to match and remove the hydrogen lines of the Paschen and Brackett series from the A0V telluric standard. The resulting telluric correction spectrum was also used for flux calibration, given the magnitudes of the A0V star from the Simbad database.

We used the FIRE spectra of SN 2012fr and its *YJH* light curves from Contreras et al. (2018) to assess the spectrophotometric accuracy of our flux calibration. With 13 epochs of simultaneous NIR spectra and light curves, we obtained a median of the differences between the colors from spectra and photometry of 0.08 and 0.03 mag for each of $Y - J$ and $J - H$ colors, respectively. This is comparable to the precision obtained in optical spectra (e.g., Silverman et al. 2012). The spectrophotometric errors in the NIR are expected to be larger, as the A0V standard stars are used as both telluric and flux standards.

In the high-throughput mode of FIRE, because the disperser includes prisms, the spacing in wavelength is not constant; rather, the logarithm of wavelength yields approximately constant spacing. As a consequence, the spectral resolution drops from blue to red. Note, however, that the detector pixels are efficiently used, as the supernova features are sampled roughly constantly in velocity space throughout the entire 0.8 to 2.5 μm wavelength coverage. Because of the non-linear wavelength spacing, we chose not to record the wavelength vector of a prism with only the first wavelength element and a wavelength spacing given in the header. Instead, the spectra were saved with wavelength, flux, and flux error at each of the 2048 detector pixels.

A quick reduction pipeline was also developed for the FIRE high-throughput mode and installed at the Magellan Baade Telescope. The quick reduction pipeline is a wrapper to the `firehose` pipeline, and uses archival flats, arcs, and telluric

Table 1
Summary of CSP-II NIR Spectroscopy of SNe Ia

SN Name	Number of NIR Spectra	Sample[a]	z_{helio}[b]	Classification by FIRE[c]
ASASSN-13ar (SN 2013dl)	3		0.0178	
ASASSN-13av	3		0.0173	
ASASSN-14ad	6	P	0.0264	
ASASSN-14eu	1		0.0227	
ASASSN-14hp	1	C	0.0389	
ASASSN-14hu	2	P	0.0216	
ASASSN-14jc	1	P	0.0113	
ASASSN-14jg	4	P	0.0148	
ASASSN-14lo	1	P	0.0199	
ASASSN-14lp	25	P	0.0051	
ASASSN-14lq	1	P	0.0262	
ASASSN-14lw	3	P	0.0209	ATel 6832
ASASSN-14me	3	P	0.018[d]	
ASASSN-14mw	3	C,P	0.0274	
ASASSN-14my	4	P	0.0205	
ASASSN-15aj	2	P	0.0109	
ASASSN-15as	2	C,P	0.0286	ATel 6920
ASASSN-15ba	2	P	0.0231	
ASASSN-15be	2	P	0.0219	
ASASSN-15bm	3	P	0.0208	
ASASSN-15cd	1	C	0.0344	
ASASSN-15eb	1	P	0.0165	
ASASSN-15fr	1	C,P	0.0334	
ASASSN-15fy	1		0.025[d]	ATel 7354
ASASSN-15ga	3	P	0.0066	
ASASSN-15go	1	P	0.0189	
ASASSN-15gr	1	P	0.0243	
ASASSN-15hf	3	P	0.0062	
ASASSN-15hx	6	P	0.008[d]	
ASASSN-15hy	6		0.025[d]	
CSS110414:145909 +071804 (SN 2011cg)	1		0.020[d]	
CSS110504:101800-023241 (SN 2011ci)	1		0.0472	
CSS110604:130707-011044 (SN 2011dj)	1		0.0185	
CSS111231:145323 +025743 (SN 2011jt)	1	P	0.0278	
CSS120224:145405 +220541 (SN 2012aq)	1	C	0.052[d]	
CSS120301:162036-102738 (SN 2012ar)	6	C,P	0.0283	CBET 3041
CSS121114:090202 +101800	1	C	0.0371	
SSS130304:114445-203141 (SN 2013ao)	6		0.0435	
CSS130315:114144-171348	1		0.050[d]	

Table 1
(Continued)

SN Name	Number of NIR Spectra	Sample[a]	z_{helio}[b]	Classification by FIRE[c]
CSS130614:233746 +144237 (SN 2013dn)	3		0.0562	
CSS131225:030144-092044	1		0.040[d]	ATel 5702
CSS150214:140955 +173155 (SN 2015bo)	1	P	0.0162	
SNhunt37 (SN 2011ae)	1		0.0060	
SNhunt46 (SN 2011be)	1		0.0340	
SNhunt177 (SN 2013az)	1	C	0.0373	CBET 3457, ATel 4935
SNhunt178 (SN 2013bc)	1	P	0.0225	CBET 3468, ATel 4948
SNhunt188 (SN 2013bz)	1	P	0.0192	
SNhunt224 (SN 2013hs)	1		0.0195	CBET 3770, ATel 5702
SNhunt229 (SN 2014D)	2	P	0.0082	CBET 3778
SNhunt281 (SN 2015bp)	9	P	0.0041	
KISS15n (SN 2015M)	1	P	0.0231[e]	
LSQ11bk	2	C	0.0403	
LSQ11ot	3	C,P	0.0273	
LSQ11pn	1	C,P	0.0327	
LSQ12bia	1		0.053[d]	
LSQ12btn	2	C	0.0542	
LSQ12cpf	2		0.0286	
LSQ12dbr	1		0.020[d]	
LSQ12frx	1		0.030[d]	
LSQ12fuk	2	P	0.0206	
LSQ12fxd	7	C,P	0.0312	
LSQ12gdj	5	C,P	0.0303	
LSQ12hzj	1	C,P	0.0334	
LSQ13pf	1	C	0.0861	ATel 4916
LSQ13ry	2	C,P	0.0299	ATel 4935
LSQ13aiz (SN 2013cs)	3	P	0.0092	
LSQ13dsm	3	C	0.0424	ATel 5714
LSQ14xi	1	C	0.0508	
LSQ14ajn (SN 2014ah)	2	P	0.0210	
LSQ14dsu	1		0.0196	
LSQ15aae	1	C	0.0516	
LSQ15adm	1		0.0723	
MASTER OT J030559.89 +043238.2	3	P	0.0282	
OGLE-2014-SN-019	1	C	0.0359	
PS1-14ra	3	C,P	0.0281	

Table 1
(Continued)

SN Name	Number of NIR Spectra	Sample[a]	z_{helio}[b]	Classification by FIRE[c]
PS15sv	3	C,P	0.0333	
PSN J13471211-2422171	1	P	0.0199	
PTF11bju	1		0.0323	
PTF11kly (SN 2011fe)	15		0.0008	
PTF11pbp (SN 2011hb)	3	C,P	0.0289	
PTF11qnr	3	P	0.0162	
PTF12ena	1		0.0166	
iPTF13asv	1		0.035[d]	
iPTF13dge	1		0.0159	
iPTF13duj	4	P	0.0170	
iPTF13dym	1	C	0.0422	
iPTF13dzm	1		0.0158	
iPTF13ebh	15	P	0.0133	ATel 5580
iPTF14aaf	1		0.0589	
iPTF14abh	1		0.0237	
iPTF14ans	1		0.0318	
iPTF14bdn	1		0.0156	
iPTF14sz	1		0.0288	
iPTF14w	7	P	0.0189	
iPTF14yw (SN 2014aa)	4	P	0.0170	
iPTF14yy	1	C	0.0431	
iPTF14fpg (SN 2014dk)	4	C,P	0.0319	
iPTF15ku	5		0.0282	
ROTSE3 J123935.1 +163512 (SN 2012G)	2	P	0.0266	
SN 2011at	2		0.0068	
SN 2011bf	2		0.0167	
SN 2011ce	3		0.0086	
SN 2011di	1		0.0147	
SN 2011iv	20	P	0.0065	
SN 2011iy	13	P	0.0043	
SN 2011jh	11	P	0.0078	
SN 2011jl	2		0.0100	
SN 2012E	4	P	0.0203	
SN 2012U	1	P	0.0197	
SN 2012Z	12		0.0071	
SN 2012ah	1	P	0.0124	
SN 2012bl	9	P	0.0187	
SN 2012bo	7	P	0.0254	
SN 2012cg	19		0.0015	ATel 4119
SN 2012db	1		0.0193	
SN 2012fr	40	P	0.0055	
SN 2012gm	2	P	0.0148	
SN 2012hd	5	P	0.0120	
SN 2012hr	12	P	0.0076	CBET 3346, ATel 4663
SN 2012ht	17	P	0.0036	
SN 2012id	3	P	0.0157	

Table 1
(Continued)

SN Name	Number of NIR Spectra	Sample[a]	z_{helio}[b]	Classification by FIRE[c]
SN 2012ij	3	P	0.0110	
SN 2013E	12	P	0.0094	
SN 2013H	4	P	0.0155	
SN 2013M	3	C,P	0.0350	
SN 2013N	1		0.0256	
SN 2013U	2	C,P	0.0345	
SN 2013aa	16	P	0.0040	
SN 2013aj	9	P	0.0091	
SN 2013ay	2	P	0.0157	CBET 3456, ATel 4935
SN 2013cg	1	P	0.0080	
SN 2013ct	7	P	0.0038	CBET 3539, ATel 5081
SN 2013dh	2		0.0134	
SN 2013dt	3		0.0241	
SN 2013fb	1		0.0170	
SN 2013fy	6	C,P	0.0309	
SN 2013fz	7	P	0.0206	
SN 2013gr	12		0.0074	CBET 3733, ATel 5612
SN 2013gv	4	C,P	0.0341	
SN 2013gy	16	P	0.0140	
SN 2013hh	7	P	0.0130	
SN 2013hl	1		0.0262	CBET 3759, ATel 5664
SN 2013hn	4	P	0.0151	
SN 2014I	5	C,P	0.0300	
SN 2014J	49		0.0007	
SN 2014Z	1	P	0.0213	CBET 3822, ATel 5959
SN 2014ao	5	P	0.0141	
SN 2014at	2	C,P	0.0322	
SN 2014ba	2	P	0.0058	
SN 2014cd	1		0.0206	
SN 2014ck	7		0.0050	
SN 2014cz	1		0.0260	CBET 3965, ATel 6442
SN 2014du	1	C,P	0.0325	
SN 2014eg	1	P	0.0186	
SN 2014ek	1		0.0231	
SN 2015F	6	P	0.0049	
SN 2015H	3		0.0125	

Notes.
[a] "C" and "P" indicate that the SN Ia is in the "Cosmology" and "Physics" samples, respectively.
[b] Host redshifts are from the NASA/IPAC Extragalactic Database (NED) or measured by CSP-II, unless otherwise noted.
[c] The column lists the ATel and CBET numbers for the SNe Ia classified by FIRE.
[d] The redshift is derived from the SN spectrum.
[e] The redshift of Coma Cluster is adopted.

spectra to automate the entire process. Because the `firehose` does not require AB pairs for background subtraction, a quick spectrum can be produced upon the completion of a single observation. Processing of a single frame takes ∼1.5 minutes. This is shorter than the typical per-frame exposure time of ∼2 minutes (without overhead). We could therefore process each frame on the fly. The 1D spectra from ABBA frames were then stacked. The quick reduction spectra typically have poor telluric correction, as there is currently no sophisticated algorithm to select or adjust an archival telluric spectrum.

The quick reduction pipeline serves several important functions. It offers the observer a check of the S/N after each successive frame and eliminates the guesswork in the number of frames required to reach the desired S/N. This has been shown to be a substantial time-saving measure, and it increased the number of targets observed per night by two- to three-fold. The quick reduction also offers the observer a check of the identity of the target under the slit within the first two frames of observation. In the case of a supernova, the features are identifiable and easily distinguished from the spectra of foreground field stars. Thus, the quick reduction also allows the efficient classification of newly discovered supernovae. Due to the rarity of early-time NIR spectra of supernovae and the valuable information they contain on the outer ejecta, we have made a concerted effort to target newly discovered and often unclassified supernovae with FIRE. With the quick reduction pipeline, FIRE becomes an efficient classification machine. Typically, a spectrum is produced from the pipeline within five minutes of acquiring the target. The S/N for a single-frame NIR spectrum is usually not adequate for science, but is often adequate for classification. Based on this, we can then decide to stay on the target or move on if the supernova does not meet our criteria for follow-up. In four years, 44 supernovae were classified using FIRE by CSP-II. The SNe Ia classified by FIRE are listed in Table 1. All classifications were immediately reported to either or both the Astronomer's Telegram (ATel) and the Central Bureau Electronic Telegrams (CBET).

2.2. GNIRS

Spectra observed with the Gemini Near InfraRed Spectrograph (GNIRS; Elias et al. 2006) on the 8.2-m Gemini North telescope were taken in the cross-dispersed mode, in combination with the short-wavelength camera, a 32 lines per mm grating, and 0.″675 slit. This configuration allowed for a wide wavelength coverage from 0.8 to 2.5 μm, divided over six orders with a resolution of $R \sim 1000$. The observing setup was similar to that described for FIRE observations. Because of the higher resolution for GNIRS, longer per-frame exposure times were used when necessary, between 240 and 300 seconds. The slit was positioned at the parallactic angle at the beginning of each observation. An A0V star was also observed before or after each set of science observations for telluric and flux calibration.

The GNIRS data were calibrated and reduced using the `XDGNIRS` pipeline, specifically developed for the reduction of GNIRS cross-dispersed data. The pipeline is partially based on the `REDCAN` pipeline for reduction of mid-IR imaging and spectroscopy from CANARICAM on the Gran Telescopio

Canarias (González-Martín et al. 2013). The steps began with pattern noise cleaning, non-linearity correction, locating the spectral orders, and flat fielding. Sky subtractions were performed for each AB pair closest in time, then the 2D spectra were stacked. Spatial distortion corrections and wavelength calibrations were applied before the 1D spectrum was extracted. Corrections for telluric absorption and simultaneous flux calibration were done with the XTELLCOR software package and the A0V telluric standard observations, using the prescription of Vacca et al. (2003). As a final step, the six orders were joined to form a single continuous spectrum.

2.3. FLAMINGOS-2

The FLAMINGOS-2 (Eikenberry et al. 2008) data were taken with the Gemini South 8.2-m telescope in long-slit mode with the *JH* grism and filter in place, in most cases using a 0.″72 slit width. This setup yielded a wavelength range of 1.0–1.8 μm and $R \sim 1000$. Again, the data were taken at the parallactic angle with a standard ABBA pattern, and with typical per-frame exposure times of 100–300 s. These long-slit data were reduced in a standard way using the F2 PyRAF package provided by Gemini Observatory, with image detrending, sky subtraction of the AB pairs, spectral extraction, wavelength calibration, and spectral combination. Telluric corrections and flux calibrations were again determined using the XTELLCOR package.

2.4. SpeX

The SpeX (Rayner et al. 2003) data obtained with the 3.0-m NASA Infrared Telescope Facility (IRTF) were generally observed in the so-called "SXD" mode, where the spectrum is cross-dispersed to obtain wavelength coverage from ~0.8–2.4 μm in a single exposure, spread over six orders. This setup yielded $R \sim 1200$ with the 0.″5 slit, the one most often used. All observations were taken with the classic ABBA technique, with typical per-frame exposures of 150 s. Furthermore, all observations were taken with the slit oriented along the parallactic angle. As with the NIR data from other spectrographs presented in this work, a A0V star was observed before or after the science observations for flux and telluric calibration.

All SpeX data were reduced using the publicly available Spextool software package (Cushing et al. 2004). This reduction proceeded in a standard way, with image detrending, order identification and sky subtraction using the AB pairs closest in time. Corrections for telluric absorption utilized the XTELLCOR software and A0V star observations (Vacca et al. 2003). After extraction and telluric correction, the 1D spectra from the six orders were rescaled and combined into a single spectrum.

3. Sample Characteristics

We obtained NIR spectra for SNe Ia in the CSP-II Physics sample to further our understanding of the origins of these explosions and to improve NIR K-corrections. The main difference between the Cosmology and Physics samples is the host-galaxy redshifts. We selected SNe Ia in the Hubble flow for the Cosmology sample, while SNe Ia in the Physics sample were required to be nearby or bright enough for high S/N, NIR spectroscopic follow-up, at least until approximately one month past maximum. For a normal SN Ia, this effectively placed an upper redshift limit at the edge of the Hubble flow, $z \sim 0.03$–0.04. Thus, the Cosmology and Physics samples are mostly independent, although there are 21 objects which belong to both samples. In total, there are 125 and 90 objects in the Cosmology and Physics samples, respectively. Details of the NIR spectroscopy sample are tabulated in Table 1, and the details of the Cosmology and Physics samples can be found in Phillips et al. (2018).

There are other differences between the samples. For SNe Ia in the Physics sample, we obtained the *BV* and *ugri* light curves with the Swope telescope and *YJH* with du Pont and Magellan whenever possible; whereas for those in the Cosmology sample, observations for *u*, *g*, and sometimes *H* bands were excluded, as these objects required considerably longer exposure times. SNe Ia in the Cosmology sample were drawn almost entirely from "blind" transient searches to minimize any bias toward more massive galaxies. These were wide-field and untargeted searches, such as the Palomar Transient Factory (PTF; Law et al. 2009), the intermediate Palomar Transient Factory (iPTF) and the La Silla Quest Low-Redshift Supernova Survey (Baltay et al. 2013), as opposed to targeted searches where a sample of pre-selected galaxies was monitored. SNe Ia from the Physics sample were drawn from both targeted (31 SNe Ia) and untargeted (59 SNe Ia) searches. For both samples, we generally required that the follow-up observations began before maximum light in the optical. The first estimation of the phase of a SN Ia was usually determined from the classification spectrum using tools like SNID (Blondin & Tonry 2007), superfit (Howell et al. 2005) or GELATO (Harutyunyan et al. 2008), but can sometimes be determined earlier with rising or falling Swope light curves.

The previous largest sample of NIR spectra of SNe Ia came from the pioneering study of Marion et al. (2009), which consists of 41 spectra obtained from SpeX on the NASA Infrared Telescope Facility (IRTF). Our goal was to improve upon this data set in several key aspects:

1. *Larger sample size.* Hsiao et al. (2007) characterized the mean optical spectral properties of SNe Ia with ~1000 spectra. The sample size of NIR spectra before CSP-II was two orders of magnitude smaller than that of optical spectra. To not only characterize the mean NIR spectral properties but also to determine the variation with light-

curve shape, the sample size of NIR spectra needed to be drastically increased.

2. *Timeseries observations*. Understanding the time evolution of NIR spectral features is important for both K-correction and physics studies. The Marion et al. (2009) sample is largely composed of single-epoch "snapshots," and is valuable for diversity studies, but contains little time evolution information.
3. *Complementary light-curve observations*. Peak absolute magnitudes and light-curve decline rates are key observables of SNe Ia. However, complementary light-curve observations are often missing for SNe Ia in the previous sample.
4. *Simultaneous optical spectra*. Optical and NIR spectra at the same phase probe different regions in the ejecta (Wheeler et al. 1998; Höflich et al. 2002) and help confirm identities of the chemical elements (e.g., Hsiao et al. 2013). Simultaneous optical and NIR spectra are also lacking in the previous sample.
5. *Improved telluric regions*. Previous NIR spectra are often marred by the heavy telluric absorptions between the *JHK* bands, mainly caused by water vapor. These wavelength regions are crucial for computing accurate K-corrections (see Section 4). The key to improved telluric corrections is increased signal in the telluric regions. Large telescope apertures and high-throughput instruments with medium resolution allow for such an improvement.

We outline below how we achieved these improvements over the previous sample.

FIRE was the main workhorse of the CSP-II NIR spectroscopy program. In the prism mode, it is capable of obtaining high S/N ($\gtrsim$20) spectra down to $H \sim 19$ mag for early-phase spectra, and down to $\sim$20 mag for the emission-line dominated, nebular-phase spectra. The high throughput of FIRE means that we were able to obtain enough counts under the strong telluric absorption lines to enable telluric corrections in most cases. For example, we recovered the Paα P-Cygni feature, which is located in the region of heavy telluric absorption between *H* and *K* bands, with 10% precision or better for 70% of spectra in our Type II sample. In Figure 1, we show an example NIR timeseries observation of SN 2012fr from pre-maximum to nebular phases, obtained entirely with FIRE. At LCO, the observing time is allotted as scheduled nights. In collaboration with the Harvard-Smithsonian Center for Astrophysics (CfA) Supernova Group, we were awarded 70 Baade nights in total during CSP-II. That is, on average, three nights per month, and this allowed continuous timeseries coverage of a large sample of SNe Ia during each Chilean summer. The timeseries was then supplemented by target of opportunity (ToO) queue mode observations from Gemini, IRTF, and the Very Large Telescope (VLT), especially during

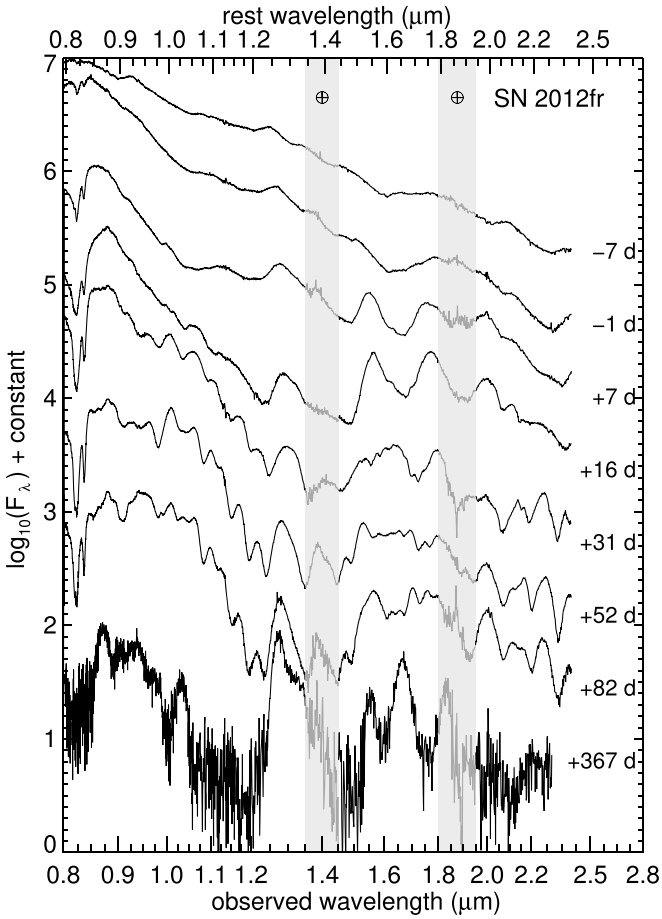

Figure 1. Sampling of NIR spectroscopic time evolution of the Type Ia SN 2012fr from pre-maximum through to transitional and nebular phases. All spectra shown were obtained with FIRE through the CSP-II NIR spectroscopy program. The phase relative to *B*-band maximum is labeled for each spectrum. The gray vertical bands mark the regions of the strongest telluric absorptions.

early phases. Whenever possible, simultaneous optical spectroscopy was obtained mainly at du Pont, Magellan, and the Nordic Optical Telescope (NOT). The vast majority of the SNe Ia had rapid-cadence (nightly) optical light curve follow-up with Swope before or at the beginning of spectroscopic observations. NIR light-curve points were obtained whenever possible with du Pont and Magellan. For a few northern objects, such as SNe 2011fe and 2014J, we relied entirely on northern facilities with NIR spectroscopic capability: Gemini North, IRTF, and the Mt. Abu 1.2-m Infrared Telescope. These objects have no complementary light curves from CSP-II.

The top panel of Figure 2 shows that there are many spectra at all phases relevant for K-corrections and template building ($\lesssim$100 days past maximum). For a few very nearby SNe Ia, the timeseries extends to the nebular phase, providing unique physical diagnostics which are described in Section 5. The bottom panel shows that the majority of SNe Ia have two

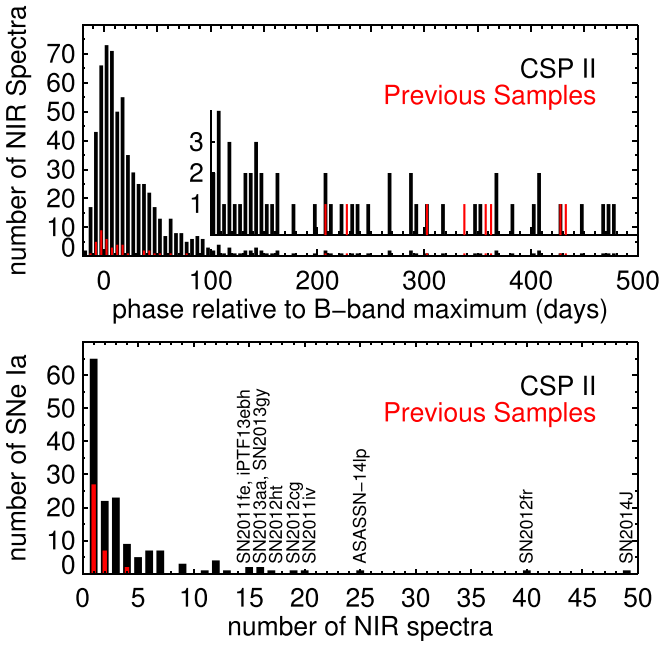

Figure 2. Number of NIR spectra at each epoch relative to *B*-band maximum (top panel) and number of SNe Ia with/without timeseries observations (bottom panel). The inset of the top panel provides a zoomed-in view of the numbers at late times. SNe Ia with 15 NIR spectra or more have their names labeled in the bottom panel. The NIR spectra of SN 2011fe (Hsiao et al. 2013) and iPTF13ebh (Hsiao et al. 2015), and a subset of the NIR spectra of SN 2011iv (Gall et al. 2018), ASASSN-14lp, and SN 2014J (Marion et al. 2015; Sand et al. 2016) were previously published.

spectra or more, providing the crucial time evolution information important for both explosion physics and K-correction studies. Figure 3 illustrates the characteristics of the SNe Ia observed in the NIR spectroscopy program. Nearly all of the SNe Ia are located within $z < 0.05$. A few more distant objects have NIR spectra taken for classification only. The vast majority of the SNe Ia have optical light-curve follow-up starting before maximum light, and the sample contains SNe Ia in the full range of light-curve-shape parameters s_{BV} (Burns et al. 2014) and $\Delta m_{15}(B)$ (Phillips 1993), determined using the updated version of `SNooPy` (Burns et al. 2011). Altogether, we obtained 661 NIR spectra of 157 SNe Ia. Within this sample, 451 NIR spectra of 90 SNe Ia are in the Physics sample with CSP-II light-curve follow-up.

The list of SNe Ia for which we obtained NIR spectra is given in Table 1. Note that there are several objects which are only in the Cosmology sample. These objects are the most distant objects in our sample, and thus in most cases only have single-epoch low S/N NIR spectra. Several objects belong to neither the Cosmology nor Physics samples for the following reasons. Some objects are of the peculiar SN 2002cx-like (e.g., Li et al. 2003; Foley et al. 2013) or "super-Chandrasekhar" (e.g. Howell et al. 2006) subtypes, which were excluded from both samples. Other objects do not have CSP-II follow-up light curves either because they exploded between observing campaigns (e.g., SN 2012cg) or they are northern objects, as mentioned previously (e.g., SN 2011fe).

Timeseries NIR spectroscopy of other SN types was also obtained, given that the existing samples are even smaller than that of SN Ia and the diagnostics in the NIR are just as powerful. Many NIR spectra of various SN types obtained by CSP-II have already been published in single-object papers: the rebrightening of SN 2009ip (Margutti et al. 2014), the Type IIb SN 2011hs (Bufano et al. 2014), the broad-lined Type Ic SN 2012ap (Milisavljevic et al. 2015), the Type Ib SN 2012au (Milisavljevic et al. 2013), the Type II SN 2012aw (Dall'Ora et al. 2014), the Type IIn SN 2012ca (Fox et al. 2015), the Type IIL SN 2013by (Valenti et al. 2015), the Type Ib/c SN 2013ge (Drout et al. 2016), as well as the SN 2002cx-like SN 2012Z (Stritzinger et al. 2015) and SN 2014ck (Tomasella et al. 2016). Note that SN 2012ca may be a SN Ia interacting with its surrounding circumstellar medium as noted by several studies (Inserra et al. 2014, 2016; Fox et al. 2015).

An atlas of the NIR spectra of supernovae of various types is plotted in Figure 4. The dominant ion species are labeled. The strong Ca II infrared triplet is present in all types of supernovae. Hydrogen Paschen and Brackett series are present in Type II supernovae. Note that Paα is located in the heavy telluric absorption between the *H* and *K* bands, therefore Paβ is often selected as the primary diagnostic in the NIR. The two strong NIR He I lines are present in Type IIb, IIn, and Ibn supernovae. One should be cognizant of the proximity between the He I λ1.0830 μm line and Paγ when identifying features in the wavelength region near 1.1 μm. Multiple Mg II lines are dominant in early Type Ia and superluminous supernova (SLSN) NIR spectra. Table 2 shows the total number of NIR spectra taken by CSP-II according to SN type and instrument used. Note that these numbers include classification spectra that do not have accompanying light curves. We discuss our use of FIRE for classification of SN types further in Section 2. For every SN type, this data set of NIR spectra will at least double the existing published sample; we hope that by opening the NIR window, the data set will further the understanding of each type of supernova.

4. K-corrections

K-corrections account for the effect of cosmological expansion upon measured magnitudes (Oke & Sandage 1968). As mentioned in the introduction, shifting SN Ia cosmology to the rest-frame NIR has the crucial advantages of largely circumventing the empirical width-luminosity relation and any uncertain dust reddening laws. This method is considered one of the most promising ways to reduce current SN Ia cosmology systematics. The potential of SNe Ia as standard candles in the NIR has been demonstrated in many studies (e.g., Krisciunas et al. 2004; Wood-Vasey et al. 2008; Folatelli et al. 2010;

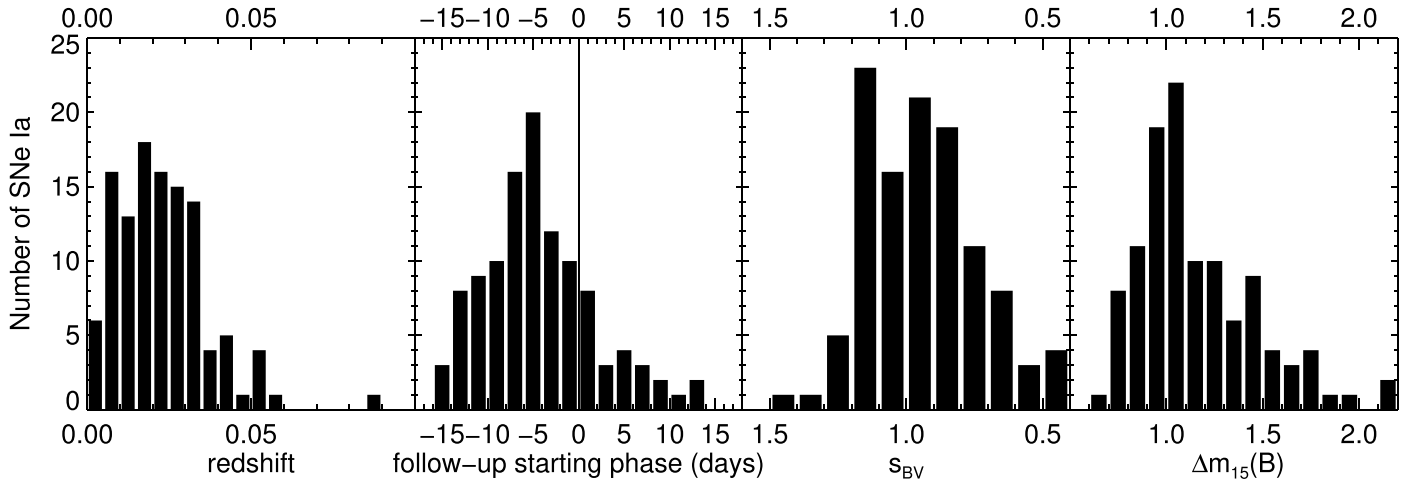

Figure 3. Characteristics of the SNe Ia in the NIR spectroscopy program. The distributions in redshift, light-curve follow-up starting phase, s_{BV}, and $\Delta m_{15}(B)$ are shown in panels from left to right.

Barone-Nugent et al. 2012; Stanishev et al. 2018; Burns et al. 2018). Furthermore, all of these studies utilized rudimentary K-corrections based on a small number of spectra. Any low-redshift experiment testing the efficacy of SNe Ia as standard candles in the NIR and any high-redshift experiment in the rest-frame NIR constraining the properties of dark energy will benefit from accurate knowledge of the diversity and time evolution of NIR spectra.

Preliminary studies of NIR K-corrections yielded the promising result of a K-correction error from the diversity in spectral features of 0.04 mag at $z = 0.08$ in the Y band (Boldt et al. 2014), but studies of the other NIR bands were limited by poor telluric corrections. It is only feasible to obtain high S/N NIR spectra for SNe Ia at $z \lesssim 0.03$. This redshift range does not allow for the sampling of the entire telluric-obscured regions. Furthermore, our CSP-II Cosmology sample for testing the efficacy of SN Ia cosmology in the NIR has a redshift range of $0.03 \lesssim z \lesssim 0.1$. This means we are relying solely on the telluric-obscured region of our NIR spectroscopic sample to K-correct the NIR light curves of our Cosmology sample, again emphasizing the importance of telluric corrections. For our FIRE sample, the high-throughput prism mode allows for the collection of enough SN photons under the water vapor absorptions in most cases (see Section 2 for details).

Another key to successful K-corrections is our ability to predict the correct spectral energy distribution with only photometric information. It has been shown that even though there is substantial spectroscopic diversity in both the optical and NIR, defining a mean spectrum eliminates systematic errors and reduces the statistical errors to an acceptable level (Hsiao et al. 2007; Hsiao 2009). There is also strong evidence that optical spectral features vary with decline rate (e.g., Nugent et al. 1995), and indications of the same behavior in the NIR (Hsiao et al. 2013). Figure 5 shows that $\Delta m_{15}(B)$ is a strong indicator of NIR spectroscopic diversity for both near- and post-maximum phases. For example, the strong Mg II $\lambda 1.0927\,\mu$m absorption feature increases in strength as we go from slow to fast-declining SNe Ia (left panel of Figure 5). The most prominent feature in the NIR for SNe Ia, the H-band break near 1.5 μm, is shown quantitatively to correlate tightly with $\Delta m_{15}(B)$ and s_{BV} (right panel of Figure 5; Hsiao et al. 2013, 2015). The accuracy of K-corrections can thus be further improved by characterizing the spectral variation with $\Delta m_{15}(B)$ or s_{BV}. Our large sample of NIR spectra will, for the first time, adequately fill the parameter space of wavelength (including telluric-obscured regions), phase, and light-curve-shape parameters.

5. Physics of SNe Ia

While the primary goal of the CSP-II NIR spectroscopy data set is to characterize SN Ia K-corrections in the NIR, the same data set is also a valuable resource for studying the physics and the progenitors of SNe Ia. The NIR spectral region has several unsaturated, strong and relatively isolated lines. Furthermore, optical and NIR spectra at the same phase probe completely different regions in the ejecta (Wheeler et al. 1998). Figure 6 shows comparison of spectral features of normal and peculiar SNe Ia in the SN 2002cx-like and the "super-Chandrasekhar" subtypes. In the optical, the spectral features between normal and peculiar SNe Ia are broadly similar. Indeed, that is why they are all classified as Type Ia. In the NIR, on the other hand, their spectral features are drastically different, revealing possible separate origins. Recent advances in the modeling of this wavelength region are also rapidly expanding the NIR tool set. We summarize some of these diagnostics here. More

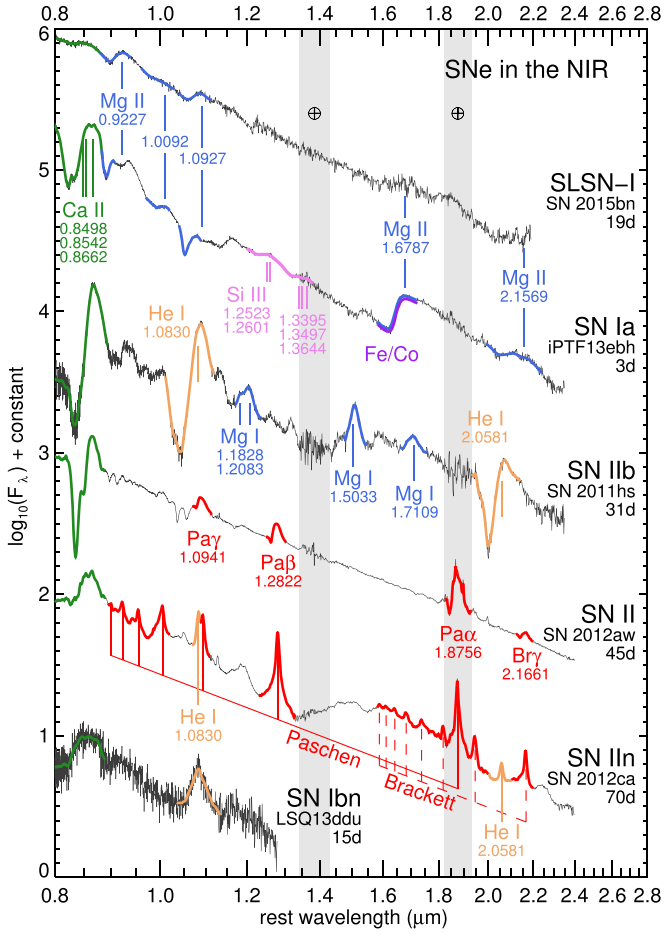

Figure 4. Atlas of NIR spectra of various SN types. The dominant ion species are labeled for comparison. The laboratory wavelengths are labeled in microns for reference and also marked on the figure as vertical lines. The supernova name and phase are labeled for each spectrum. The phases are relative to maximum light, except for that of SN 2012aw, which is relative to explosion. The gray vertical bands mark the regions of the strongest telluric absorptions. All spectra shown were taken with FIRE as part of the CSP-II NIR spectroscopy program. Spectra of iPTF13ebh (Hsiao et al. 2015), SN 2011hs (Bufano et al. 2014), SN 2012aw (Dall'Ora et al. 2014), and SN 2012ca (Fox et al. 2015) were published previously. FIRE spectra of the SLSN-I SN 2015bn and the Type Ibn LSQ13ddu are shown for the first time.

detailed analysis for each will be presented in forthcoming papers.

5.1. *Unburned Material via C I λ 1.0693 μm*

The general consensus for the origin of a SN Ia is the thermonuclear explosion of a carbon–oxygen white dwarf (Hoyle & Fowler 1960). Because oxygen is also produced from carbon burning, carbon provides the most direct probe of the primordial material from the progenitor white dwarf. The quantity, distribution and incidence of unburned carbon provides important constraints for explosion models. The Chandrasekhar-mass DDT scenario predicts nearly complete carbon burning for normal SNe Ia (Kasen et al. 2009) and increasing amounts of surviving carbon for fainter SNe Ia (Höflich et al. 2002). The pulsating class of DDT models also leaves large amounts of unburned carbon, even for normal objects (Hoeflich et al. 1995). On the other hand, unburned carbon is not expected to survive in the explosions of sub-Chandrasekhar-mass white dwarfs, except for a small amount below the outer layer of iron-group elements produced during the surface helium detonation (e.g., Fink et al. 2010).

Until recently, the study of unburned material had mainly relied on the optical C II λ0.6580 μm line, which is marred by several selection biases. It is a weak spectral feature situated near the emission component of the strong Si II λ0.6355 μm P-Cygni profile, such that high-velocity carbon may be buried in the silicon absorption and measured velocities suffer from limb variation effects (Hoeflich 1990). It also tends to fade rapidly after explosion, which makes obtaining a complete sample rather difficult. Surveys of large optical spectroscopic samples found that 20%–30% of pre-maximum spectra show C II signatures (Thomas et al. 2011; Parrent et al. 2011; Folatelli et al. 2012; Silverman & Filippenko 2012).

In contrast to the weak and fast-fading nature of the optical C II λ0.6580 μm line, the NIR C I λ1.0693 μm line may be much stronger. Also, it increases in strength toward maximum light for normal-bright objects (Hsiao et al. 2013). The delayed onset of the NIR C I line may be a manifestation of the recombination from C II to C I as the ejecta expands and cools, and highlights the potential of the NIR C I line to secure more representative properties of unburned material in SNe Ia. With the aid of SYNAPPS (Thomas et al. 2011), the NIR C I feature has been identified in several SNe Ia with a large range of peak magnitudes (Figure 7; Hsiao et al. 2013, 2015; Marion et al. 2015). While the current number of NIR carbon detections is small, the incidence of carbon appears to be ubiquitous, with the fast-declining, fainter SNe Ia having the strongest C I lines. This preliminary result appears to contradict the claim of Blondin et al. (2017) that fast-declining faint SNe Ia result from the explosions of sub-Chandrasekhar-mass white dwarfs. However, more detailed analysis is needed to determine whether the small amount of unburned carbon beneath the surface iron-peak layer in sub-Chandrasekhar-mass models can produce the observed carbon features. With the CSP-II sample of ∼120 pre-maximum NIR spectra of ∼50 SNe Ia, we aim to characterize the properties of unburned material in SNe Ia in an unbiased fashion.

In the sub-Chandrasekhar helium detonation scenario, unburned helium left over from the surface helium layer can potentially produce strong NIR He I λ1.0830 and λ2.0581 μm lines, as we have shown for other supernova types in Figure 4. Boyle et al. (2017) explored these features, and the possibility of confusion with the C I λ1.0693 μm line. This emphasizes the importance of identifying multiple lines of the same ion when searching for unburned carbon, as was done for SN 1999by

Table 2
Number of NIR Spectra by Instrument and SN Type

Telecope	Instrument	Ia	2002cx-like	Ibc	II	IIn	SLSN	Others	Total
Magellan Baade	FIRE	450	27	97	79	35	9	4	701
Magellan Clay	MMIRS	7	1	2	1	0	0	1	12
Gemini North	GNIRS	63	7	0	0	0	0	0	70
Gemini South	FLAMINGOS-2	17	0	0	1	0	0	0	18
IRTF	SpeX	40	1	6	9	2	0	0	58
VLT	ISAAC	8	4	0	0	0	0	0	12
NTT	SofI	4	1	2	0	0	0	0	7
Mt Abu	NICS	31	0	0	0	0	0	0	31
Total spectra		620	41	107	90	37	9	5	909
Total SNe		149	8	42	31	12	5	2	249

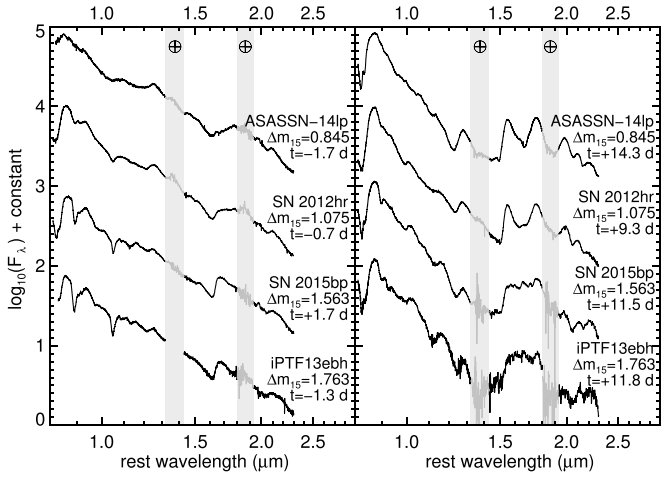

Figure 5. Comparison of SN Ia NIR spectra of various decline rate $\Delta m_{15}(B)$ values. The left and right panels show the spectra near maximum and 1–2 weeks past maximum, respectively. The SN name, $\Delta m_{15}(B)$, and spectral phase are labeled for each spectrum. The gray vertical bands mark the regions of the strongest telluric absorptions. The spectral diversity in the NIR is strongly correlated with the light-curve shape.

(Höflich et al. 2002) and iPTF13ebh (Hsiao et al. 2015). Note that both of these objects are fast-declining, fainter SNe Ia, which tend to show the strongest C I lines.

5.2. Radioactive Nickel via H-band Break

A dramatic shift in the amount of line blanketing from iron-group elements takes place near 1.5 μm and produces the strong *H*-band break after maximum light (Wheeler et al. 1998). Observationally, SNe Ia are found to have uniform evolution of the *H*-band features. The *H*-band break appears at ~3 days past maximum and rapidly increases in strength as the feature formed by iron-peak elements becomes fully exposed at ~12 days past maximum. It then steadily decreases in strength at very similar rates for all SNe Ia out to approximately one month past maximum. The maximum size of the *H*-band break, when the iron-peak complex is fully exposed, is also found to correlate with the SN Ia light-curve decline rate $\Delta m_{15}(B)$ (Hsiao et al. 2013).

The size and velocity shift of the *H*-band break probes the amount and distribution of radioactive ^{56}Ni, and the time evolution of the *H*-band break is related to the amount of intermediate-mass elements acting as the "shielding mass." In the Chandrasekhar-mass DDT scenario, for example, there is an increasing amount of intermediate-mass elements produced with decreasing ^{56}Ni production, while for the sub-Chandrasekhar-mass He detonation scenario, the ^{56}Ni production increases with the total mass. Each scenario therefore produces a unique rate at which the *H*-band complex is exposed and a specific correlation between the strength of the *H*-band break and $\Delta m_{15}(B)$. CSP-II has gathered ~300 NIR spectra of ~120 SNe Ia between maximum light and +30 days. We aim to use this sample to confirm the strong correlation with decline rate discovered by Hsiao et al. (2013, 2015) with only 10 SNe Ia, in addition to improving the measurements of the rate at which the *H*-band complex is exposed, which is currently poorly constrained.

5.3. Companion Signature via Paβ and He I

The nature of the companion star in the progenitor system is still a mystery. The collision between the SN Ia ejecta and the companion may produce detectable signatures that can be used to place constraints on the properties of the companion star (e.g., Kasen 2010), although predictions on whether the signature is detectable may be model dependent (Cumming et al. 1996). In particular, if the companion star has a hydrogen or helium-rich envelope in a single-degenerate system, the envelope is expected to be stripped away during the collision and be embedded deep within the low-velocity part of the expanding SN Ia ejecta (Marietta et al. 2000). This has been suggested to produce Hα in late-time spectra, beyond 200 days. So far, none have been detected in nearby SNe Ia (e.g., Mattila et al. 2005; Shappee et al. 2013; Sand et al. 2018). More recently, Maeda et al. (2014) suggested that NIR Paβ

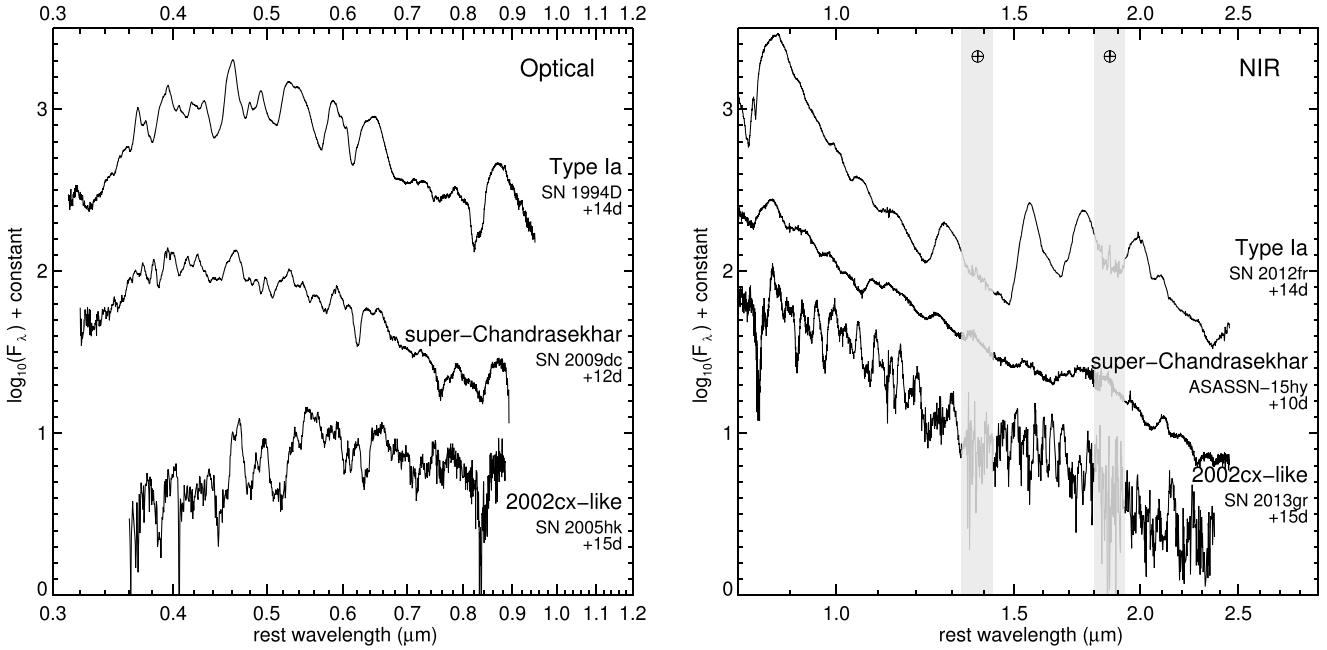

Figure 6. Comparison of spectral features of normal and peculiar SNe Ia. Left and right panels show spectra in the optical and NIR, respectively. In the right panel, the gray vertical bands mark the regions of the strongest telluric absorptions. In the optical, the spectral features between normal and peculiar SNe Ia are broadly similar. Indeed, that is why they are all classified as Type Ia. In the NIR, on the other hand, their spectral features are drastically different, revealing possible separate origins. The optical spectra of SNe 1994D (Ruiz-Lapuente et al. 1997), 2009dc (Taubenberger et al. 2011), and 2005hk (Phillips et al. 2007) were previously published. The GNIRS spectrum of ASASSN-15hy and FIRE spectra of SNe 2012fr and 2013gr were obtained as part of the CSP-II NIR spectroscopy program.

companion signature is potentially much stronger than Hα, and it appears much earlier. The strong NIR He I lines can also be easily detected (Botyánszki et al. 2018). These desirable properties could lead to the first detection of embedded hydrogen or helium stripped from the companion star or at least place stronger constraints on its absence. We published the first searches for the Paβ emission in the NIR. Although these were also non-detections, they placed upper limits of $<0.1\,M_{\odot}$ of stripped hydrogen from the companion stars of SNe 2014J (Sand et al. 2016) and 2017cbv (Hosseinzadeh et al. 2017).

Two main challenges for the detection of these so-far elusive hydrogen lines are (1) viewing angle effects and (2) diversity of the SN Ia feature underneath the hydrogen emissions, both requiring a statistically significant sample. The CSP-II data set with ~100 NIR spectra of ~50 SNe Ia between one and two months past maximum currently is the best data set for such a study.

5.4. Neutron Content via [Ni II] 1.939 μm

Recent theoretical studies of SNe Ia undergoing the transition from the photospheric to nebular phase identified a strong NIR emission feature as [Ni II] λ1.939 μm (Friesen et al. 2014; Wilk et al. 2018), although this identification had been disputed by Blondin et al. (2015). At such late phases, all of the radioactive ^{56}Ni has decayed into ^{56}Co. If the observed line is indeed attributed to [Ni II], it must then be produced by the stable isotope ^{58}as we are likely probing the neutron content in the inner region at these late phases, the detection of [Ni II] features would indicate high-density burning (Thielemann et al. 1986; Iwamoto et al. 1999) and may be less sensitive to the metallicity of the progenitor (Höflich et al. 1998; Timmes et al. 2003) or the neutronization in the simmering phase (Piro & Bildsten 2008). High-density burning is a hallmark of Chandrasekhar-mass DDT models, while sub-Chandrasekhar explosion models tend to underproduce stable neutron-rich elements (Seitenzahl et al. 2013).

Spectra in the NIR obtained during the transition to nebular phase are still quite rare. Furthermore, the [Ni II] λ1.939 μm line is close to the strong telluric water vapor absorptions between *H* and *K* bands. Friesen et al. (2014) gathered four NIR spectra from the literature and two new observations of SN 2014J between 50 and 100 days past explosion. Only the two NIR spectra of SN 2014J had adequate wavelength coverage, telluric correction, and S/N to detect the presence of this feature. The feature was also reported in the NIR nebular spectra of SN 2014J obtained by Dhawan et al. (2018). With the CSP-II sample of ~100 transitional to nebular phase NIR spectra of ~40 SNe Ia, we aim to analyze the diversity in the properties of this feature. Figure 1 shows an example of our timeseries data, taken of SN 2012fr. The feature reported by

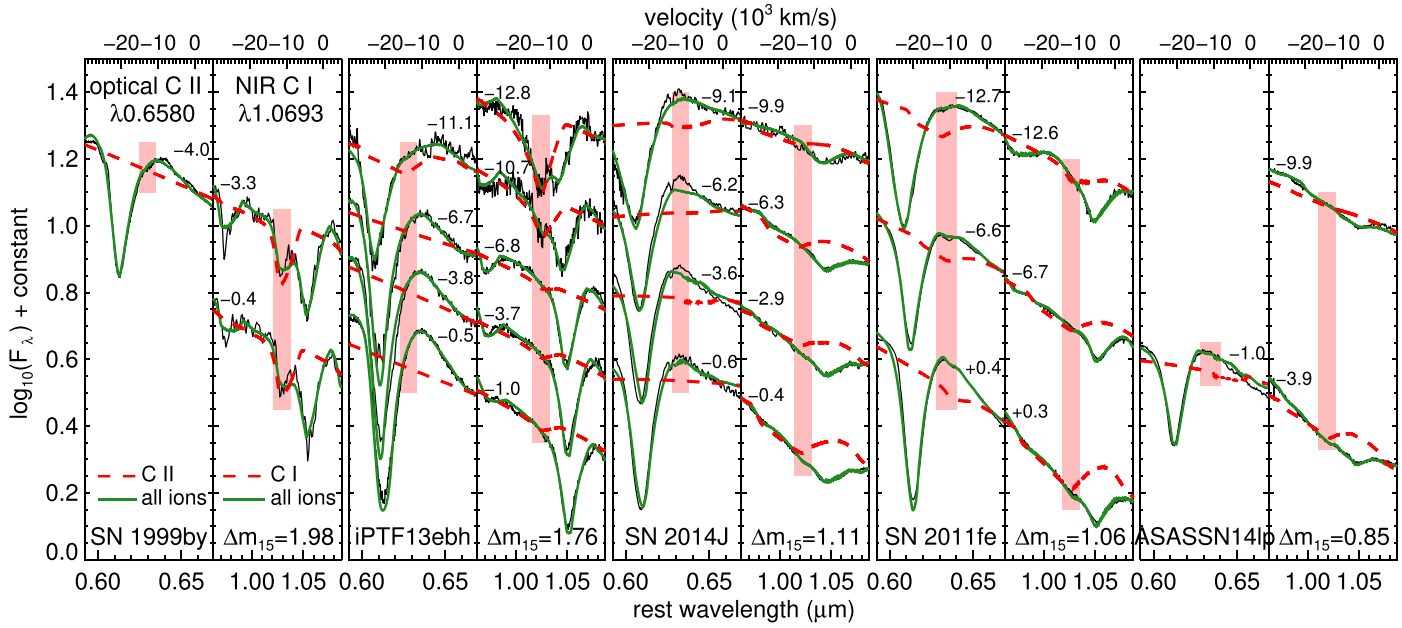

Figure 7. Comparison between the optical C II λ0.6580 μm and the NIR C I λ1.0693 μm lines of the five SNe Ia with C I detections. This plot is an expansion of Figure 10 in Hsiao et al. (2015) with the addition of the slow-declining ASASSN-14lp. The optical/NIR pair is selected such that the spectra are close in phase for each SN Ia. The phases relative to *B* maximum are labeled. The velocity axes are plotted with respect to each carbon line. The SYNAPPS (Thomas et al. 2011) fits are plotted in green solid curves. We also plot the isolated influence from the carbon lines of the same fits in red dashed curves. The vertical pink bars provide guides to the locations of the carbon absorption troughs, or approximately where they would be if the features are indeed present. Except at the very early epoch of SN 2011fe, the NIR C I line is always stronger than the optical C II line.

Friesen et al. (2014) was indeed also present in SN 2012fr and evolved to be its strongest feature in the *K* band during the transitional phase (+82 days past *B* maximum in Figure 1). By the nebular phase, the feature became much weaker, and our nebular spectrum at +367 days unfortunately did not have a high enough S/N to confirm the presence of this feature. Further study on the modeling side is also planned to secure the identification of this line.

5.5. Central Density and Magnetic Field via [Fe II] 1.644 μm

Nebular-phase observations of line profiles can reveal the isotopic structure of the inner region. In particular, the forbidden [Fe II] 1.644 μm line is ideal for such studies, as it is strong and unblended. It can be used to measure the properties of the progenitor system and explosion, such as asphericity, initial central density, and magnetic field (Penney & Hoeflich 2014; Diamond et al. 2015, 2018). Up to 200 days past explosion, the line profile can be used to analyze the overall chemical and density structure of the exploding white dwarf without considering the magnetic field, as the energy deposition by gamma-ray photons dominates. Measurements of the central density can lead us to the accretion history of the pre-explosion white dwarf (Nomoto et al. 1984) and the amount of stable ^{58}Ni produced (Höflich et al. 2006). Note that updated electron capture rates (e.g., Brachwitz et al. 2000) no longer yield enough stable iron-group elements to produce the "flat-top" profiles emphasized by Maguire et al. (2018), except in the most extreme cases. Rather, increasing central density widens the line width of the [Fe II] 1.644 μm line and the effects can be measured with moderate S/N nebular spectra (Diamond et al. 2015, 2018). Going to even later phases, beyond one year past explosion, the time evolution of the line profile is sensitive to positron transport effects. The escape probability of the positrons, which directly influences the width of the [Fe II] line, depends strongly on the size and the morphology of the magnetic fields.

For the Chandrasekhar-mass DDT scenario, 3D hydrodynamical simulations consistently predict large-scale mixing of the ejecta due to Rayleigh-Taylor instabilities during the deflagration burning phase (Röpke et al. 2006), producing results which are inconsistent with observations. Recently, Hristov et al. (2018) found that the magnetic field plays an important role during this burning phase. Their magnetohydrodynamical study showed increasing suppression of the instabilities starting at $\sim 10^9$ G. Such magnetic fields may be generated during the pre-explosive carbon-simmering phase of Chandrasekhar-mass explosions (Piro & Chang 2008). Current measurements based on a handful of NIR nebular spectra of nearby SNe Ia indicated relatively high central densities and high magnetic fields (e.g., Penney & Hoeflich 2014; Diamond et al. 2015). We are

extending the analysis to the CSP-II sample of ~20 NIR spectra of seven SNe Ia at phases beyond 200 days past explosion. Meanwhile, ongoing programs at Gemini and LCO, as part of CSP-II, continue to monitor the time evolution of the [Fe II] line profile of nearby SNe Ia.

6. Summary

This paper presents an introduction to the CSP-II NIR spectroscopy program, which we carried out from 2011 to 2015. This project represents an important step for any current and future SN Ia cosmological experiments based on the rest-frame NIR. These experiments have been shown to reduce errors by effectively circumventing the uncertain dust laws and empirical width-luminosity relation. The data set collected is unique in its large sample size; timeseries observations; complementary light-curve and optical spectroscopic observations; and improvement in the telluric regions. Such a sample makes it possible to quantify the representative NIR spectroscopic time evolution and diversity of SNe Ia, allowing NIR cosmological experiments to reach their true potential. By exploring the NIR wavelength window, many diagnostics for the explosion mechanisms and the progenitor systems of SNe Ia also become available. Understanding the origins of these events represents a second and independent way to reduce systematic errors in SN Ia cosmology. While our focus is on normal SNe Ia for cosmological studies, comparisons of NIR spectroscopic features between normal and peculiar SNe Ia (Figure 6), and between supernovae of various types (Figure 4), highlight the identifying features and offer clues to the origins of these events.

We are pleased to acknowledge the following individuals (in alphabetical order) for their assistance in obtaining the NIR spectroscopic data set: Y. Beletsky, G. Blanc, T. Dupuy, N. Elias-Rosa, R. Foley, L. W. Hsiao, B. Madore, A. Monson, E. Newton, D. Osip, P. Palunas, J. L. Prieto, M. Rouch, S. Schulze, and M. Turatto. We also thank the Las Campanas technical staff for their continued support over the years. The CSP-II has been supported by NSF grants AST-1008343, AST-1613426, AST-1613455, and AST-1613472, as well as the Danish Agency for Science and Technology and Innovation through a Sapere Aude Level 2 grant. M.S. acknowledges funding by a research grant (13261) from VILLUM FONDEN. Research by D.J.S. is supported by NSF grants AST-1821967, 1821987, 1813708, and 1813466. N.B.S. and K.K. acknowledge support from the The George P. and Cynthia Woods Mitchell Institute for Fundamental Physics and Astronomy. T.D. is supported by an appointment to the NASA Postdoctoral Program at the Goddard Space Flight Center, administered by Universities Space Research Association under contract with NASA. L.W. acknowledges the support by the Chinese Academy of Sciences (CAS), through a grant to the CAS South America Center for Astronomy (CASSACA) in Santiago, Chile. The bulk of the data presented here was obtained with the 1 m Swope, 2.5 m du Pont, and the 6.5 m Magellan Telescopes at the Las Campanas Observatory. Observations were also obtained at the Gemini Observatory (program IDs: GN-2011B-Q-68, GN-2012A-Q-59, GN-2012A-Q-69, GN-2013B-Q-76, GN-2014A-Q-52, GN-2014B-Q-13, GN-2014B-Q-70, GN-2015B-Q-7, and GS-2015B-Q-5), which is operated by the Association of Universities for Research in Astronomy, Inc., under a cooperative agreement with the NSF on behalf of the Gemini partnership: the National Science Foundation (United States), the National Research Council (Canada), CONICYT (Chile), Ministerio de Ciencia, Tecnología e Innovación Productiva (Argentina), and Ministério da Ciência, Tecnologia e Inovação (Brazil). Also based on observations collected at the European Organisation for Astronomical Research in the Southern Hemisphere under ESO programme 088.D-0222. This research used resources of the National Energy Research Scientific Computing Center (NERSC), a U.S. Department of Energy Office of Science User Facility operated under contract No. DE-AC02-05CH11231. We have also made use of the NASA/IPAC Extragalactic Database (NED) which is operated by the Jet Propulsion Laboratory, California Institute of Technology, under contract with the National Aeronautics and Space Administration.

Facilities: Magellan Baade (FIRE), du Pont (WFCCD) Gemini North (GNIRS near-infrared spectrograph), Gemini South (FLAMINGOS-2), VLT (ISAAC), IRTF (SpeX), NOT (ALFOSC), La Silla-QUEST, CRTS, PTF, iPTF, OGLE, ASAS-SN, PS1, KISS, ISSP, MASTER, SMT.

Software: `firehose` (Simcoe et al. 2013), `GELATO` (Harutyunyan et al. 2008), `SNID` (Blondin & Tonry 2007), `Spextool` (Cushing et al. 2004), `superfit` (Howell et al. 2005), `SYNAPPS` (Thomas et al. 2011), `XDGNIRS`, `xtellcor` (Vacca et al. 2003).

ORCID iDs

E. Y. Hsiao (蕭亦麒) https://orcid.org/0000-0003-1039-2928
M. M. Phillips https://orcid.org/0000-0003-2734-0796

References

Baltay, C., Rabinowitz, D., Hadjiyska, E., et al. 2013, PASP, 125, 683
Barone-Nugent, R. L., Lidman, C., Wyithe, J. S. B., et al. 2012, MNRAS, 425, 1007
Betoule, M., Kessler, R., Guy, J., et al. 2014, A&A, 568, A22
Blondin, S., Dessart, L., & Hillier, D. J. 2015, MNRAS, 448, 2766
Blondin, S., Dessart, L., Hillier, D. J., & Khokhlov, A. M. 2017, MNRAS, 470, 157
Blondin, S., & Tonry, J. L. 2007, ApJ, 666, 1024
Boldt, L. N., Stritzinger, M. D., Burns, C., et al. 2014, PASP, 126, 324
Botyánszki, J., Kasen, D., & Plewa, T. 2018, ApJ, 852, L6
Boyle, A., Sim, S. A., Hachinger, S., & Kerzendorf, W. 2017, A&A, 599, A46
Brachwitz, F., Dean, D. J., Hix, W. R., et al. 2000, ApJ, 536, 934
Bufano, F., Pignata, G., Bersten, M., et al. 2014, MNRAS, 439, 1807

Burns, C. R., et al. 2018, arXiv:1809.06381
Burns, C. R., Stritzinger, M., Phillips, M. M., et al. 2011, AJ, 141, 19
Burns, C. R., Stritzinger, M., Phillips, M. M., et al. 2014, ApJ, 789, 32
Conley, A., Guy, J., Sullivan, M., et al. 2011, ApJS, 192, 1
Contreras, C., Hamuy, M., Phillips, M. M., et al. 2010, AJ, 139, 519
Contreras, C., Phillips, M. M., Burns, C. R., et al. 2018, ApJ, 859, 24
Cumming, R. J., Lundqvist, P., Smith, L. J., Pettini, M., & King, D. L. 1996, MNRAS, 283, 1355
Cushing, M. C., Vacca, W. D., & Rayner, J. T. 2004, PASP, 116, 362
Dall'Ora, M., Botticella, M. T., Pumo, M. L., et al. 2014, ApJ, 787, 139
Dhawan, S., Flörs, A., Leibundgut, B., et al. 2018, arXiv:1805.02420
Diamond, T. R., Hoeflich, P., & Gerardy, C. L. 2015, ApJ, 806, 107
Diamond, T. R., Hoeflich, P., Hsiao, E. Y., et al. 2018, ApJ, 861, 119
Drout, M. R., Milisavljevic, D., Parrent, J., et al. 2016, ApJ, 821, 57
Eikenberry, S., Elston, R., Raines, S. N., et al. 2008, Proc. SPIE, 7014, 70140V
Elias, J. H., Joyce, R. R., Liang, M., et al. 2006, Proc. SPIE, 6269, 62694C
Filippenko, A. V. 1982, PASP, 94, 715
Fink, M., Röpke, F. K., Hillebrandt, W., et al. 2010, A&A, 514, A53
Folatelli, G., Phillips, M. M., Burns, C. R., et al. 2010, AJ, 139, 120
Folatelli, G., Phillips, M. M., Morrell, N., et al. 2012, ApJ, 745, 74
Foley, R. J., Challis, P. J., Chornock, R., et al. 2013, ApJ, 767, 57
Fox, O. D., Silverman, J. M., Filippenko, A. V., et al. 2015, MNRAS, 447, 772
Freedman, W. L., Burns, C. R., Phillips, M. M., et al. 2009, ApJ, 704, 1036
Friesen, B., Baron, E., Wisniewski, J. P., et al. 2014, ApJ, 792, 120
Gall, C., Stritzinger, M. D., Ashall, C., et al. 2018, A&A, 611, A58
González-Martín, O., Rodríguez-Espinosa, J. M., Díaz-Santos, T., et al. 2013, A&A, 553, A35
Hachinger, S., Mazzali, P. A., Tanaka, M., Hillebrandt, W., & Benetti, S. 2008, MNRAS, 389, 1087
Hamuy, M., Folatelli, G., Morrell, N. I., et al. 2006, PASP, 118, 2
Harutyunyan, A. H., Pfahler, P., Pastorello, A., et al. 2008, A&A, 488, 383
Hoeflich, P. 1990, A&A, 229, 191
Höflich, P. 1995, ApJ, 443, 89
Höflich, P., Gerardy, C. L., Fesen, R. A., & Sakai, S. 2002, ApJ, 568, 791
Höflich, P., Gerardy, C. L., Marion, H., & Quimby, R. 2006, NewAR, 50, 470
Hoeflich, P., Hsiao, E. Y., Ashall, C., et al. 2017, ApJ, 846, 58
Hoeflich, P., Khokhlov, A. M., & Wheeler, J. C. 1995, ApJ, 444, 831
Höflich, P., Wheeler, J. C., & Thielemann, F. K. 1998, ApJ, 495, 617
Horne, K. 1986, PASP, 98, 609
Hosseinzadeh, G., Sand, D. J., Valenti, S., et al. 2017, ApJ, 845, L11
Howell, D. A., Sullivan, M., Nugent, P. E., et al. 2006, Natur, 443, 308
Howell, D. A., Sullivan, M., Perrett, K., et al. 2005, ApJ, 634, 1190
Hoyle, F., & Fowler, W. A. 1960, ApJ, 132, 565
Hristov, B., Collins, D. C., Hoeflich, P., Weatherford, C. A., & Diamond, T. R. 2018, ApJ, 858, 13
Hsiao, E. Y. 2009, Ph.D. thesis, Univ. Victoria
Hsiao, E. Y., Burns, C. R., Contreras, C., et al. 2015, A&A, 578, A9
Hsiao, E. Y., Conley, A., Howell, D. A., et al. 2007, ApJ, 663, 1187
Hsiao, E. Y., Marion, G. H., Phillips, M. M., et al. 2013, ApJ, 766, 72
Iben, I., Jr., & Tutukov, A. V. 1984, ApJS, 54, 335
Inserra, C., Inserra, C., Fraser, M., Smartt, S. J., et al. 2016, MNRAS, 459, 2721
Inserra, C., Smartt, S. J., Scalzo, R., et al. 2014, MNRAS, 437, L51
Iwamoto, K., Brachwitz, F., Nomoto, K., et al. 1999, ApJS, 125, 439
Kasen, D. 2006, ApJ, 649, 939
Kasen, D. 2010, ApJ, 708, 1025
Kasen, D., Röpke, F. K., & Woosley, S. E. 2009, Natur, 460, 869
Kattner, S., Leonard, D. C., Burns, C. R., et al. 2012, PASP, 124, 114
Kelson, D. D. 2003, PASP, 115, 688
Khokhlov, A. M. 1991, A&A, 245, 114
Krisciunas, K., Contreras, C., Burns, C. R., et al. 2017, AJ, 154, 211
Krisciunas, K., Phillips, M. M., & Suntzeff, N. B. 2004, ApJ, 602, L81
Law, N. M., Kulkarni, S. R., Dekany, R. G., et al. 2009, PASP, 121, 1395
Li, W., Filippenko, A. V., Chornock, R., et al. 2003, PASP, 115, 453
Maeda, K., Kutsuna, M., & Shigeyama, T. 2014, ApJ, 794, 37
Maguire, K., Sim, S. A., Shingles, L., et al. 2018, MNRAS, 477, 3567
Mandel, K. S., Narayan, G., & Kirshner, R. P. 2011, ApJ, 731, 120
Margutti, R., Milisavljevic, D., Soderberg, A. M., et al. 2014, ApJ, 780, 21
Marietta, E., Burrows, A., & Fryxell, B. 2000, ApJS, 128, 615
Marion, G. H., Höflich, P., Gerardy, C. L., et al. 2009, AJ, 138, 727
Marion, G. H., Sand, D. J., Hsiao, E. Y., et al. 2015, ApJ, 798, 39
Mattila, S., Lundqvist, P., Sollerman, J., et al. 2005, A&A, 443, 649
Milisavljevic, D., Margutti, R., Parrent, J. T., et al. 2015, ApJ, 799, 51
Milisavljevic, D., Soderberg, A. M., Margutti, R., et al. 2013, ApJ, 770, L38
Nomoto, K. 1982, ApJ, 253, 798
Nomoto, K., Thielemann, F.-K., & Yokoi, K. 1984, ApJ, 286, 644
Nugent, P., Phillips, M., Baron, E., Branch, D., & Hauschildt, P. 1995, ApJ, 455, L147
Oke, J. B., & Sandage, A. 1968, ApJ, 154, 21
Parrent, J. T., Thomas, R. C., Fesen, R. A., et al. 2011, ApJ, 732, 30
Penney, R., & Hoeflich, P. 2014, ApJ, 795, 84
Perlmutter, S., Aldering, G., Goldhaber, G., et al. 1999, ApJ, 517, 565
Persson, S. E., Murphy, D. C., Smee, S., et al. 2013, PASP, 125, 654
Phillips, M. M. 1993, ApJ, 413, L105
Phillips, M. M., Li, W., Frieman, J. A., et al. 2007, PASP, 119, 360
Phillips, M. M., et al. 2018, PASP, 131, 014001
Piro, A. L., & Bildsten, L. 2008, ApJ, 673, 1009
Piro, A. L., & Chang, P. 2008, ApJ, 678, 1158
Rayner, J. T., Toomey, D. W., Onaka, P. M., et al. 2003, PASP, 115, 362
Röpke, F. K., Gieseler, M., Reinecke, M., Travaglio, C., & Hillebrandt, W. 2006, A&A, 453, 203
Riess, A. G., Filippenko, A. V., Challis, P., et al. 1998, AJ, 116, 1009
Ruiz-Lapuente, P., Canal, R., & Isern, J. 1997, NATO Advanced Science Institutes (ASI) Series C, 486
Sand, D. J., Graham, M. L., Botyánszki, J., et al. 2018, ApJ, 863, 24
Sand, D. J., Hsiao, E. Y., Banerjee, D. P. K., et al. 2016, ApJ, 822, L16
Scolnic, D. M., Jones, D. O., Rest, A., et al. 2018, ApJ, 859, 101
Seitenzahl, I. R., Cescutti, G., Röpke, F. K., Ruiter, A. J., & Pakmor, R. 2013, A&A, 559, L5
Shappee, B. J., Stanek, K. Z., Pogge, R. W., Garnavich, P. M., et al. 2013, ApJ, 762, L5
Silverman, J. M., & Filippenko, A. V. 2012, MNRAS, 425, 1917
Silverman, J. M., Foley, R. J., Filippenko, A. V., et al. 2012, MNRAS, 425, 1789
Simcoe, R. A., Burgasser, A. J., Schechter, P. L., et al. 2013, PASP, 125, 270
Stanishev, V., Goobar, A., Amanullah, R., et al. 2018, A&A, 615, A45
Stritzinger, M. D., Anderson, J. P., Contreras, C., et al. 2018, A&A, 609, A134
Stritzinger, M. D., Phillips, M. M., Boldt, L. N., et al. 2011, AJ, 142, 156
Stritzinger, M. D., Valenti, S., Hoeflich, P., et al. 2015, A&A, 573, A2
Suzuki, N., Rubin, D., Lidman, C., et al. 2012, ApJ, 746, 85
Taubenberger, S., Benetti, S., Childress, M., et al. 2011, MNRAS, 412, 2735
Thielemann, F.-K., Nomoto, K., & Yokoi, K. 1986, A&A, 158, 17
Thomas, R. C., Aldering, G., Antilogus, P., et al. 2011, ApJ, 743, 27
Thomas, R. C., Nugent, P. E., & Meza, J. C. 2011, PASP, 123, 237
Timmes, F. X., Brown, E. F., & Truran, J. W. 2003, ApJ, 590, L83
Tomasella, L., Cappellaro, E., Benetti, S., et al. 2016, MNRAS, 459, 1018
Vacca, W. D., Cushing, M. C., & Rayner, J. T. 2003, PASP, 115, 389
Valenti, S., Sand, D., Stritzinger, M., et al. 2015, MNRAS, 448, 2608
Webbink, R. F. 1984, ApJ, 277, 355
Wheeler, J. C., Höflich, P., Harkness, R. P., & Spyromilio, J. 1998, ApJ, 496, 908
Whelan, J., & Iben, I., Jr. 1973, ApJ, 186, 1007
Wilk, K. D., Hillier, D. J., & Dessart, L. 2018, MNRAS, 474, 3187
Wood-Vasey, W. M., Friedman, A. S., Bloom, J. S., et al. 2008, ApJ, 689, 377